Measuring arterial pulsatility with Dynamic Inflow MAgnitude Contrast (DIMAC)

Joseph R. Whittaker[1,2]*, Fabrizio Fasano[3], Marcello Venzi[1], Patrick Liebig[4], Daniel Gallichan[5], and Kevin Murphy[1]

1. *Cardiff University Brain Research Imaging Centre (CUBRIC), School of Physics and Astronomy, Cardiff University, Cardiff, CF24 4HQ, United Kingdom*
2. *Max Planck Institute for Human Cognitive and Brain Sciences, Leipzig, Germany*
3. *Siemens Healthcare Ltd, Camberly, United Kingdom*
4. *Siemens Healthcare GmbH, Erlangen, Germany*
5. *CUBRIC, School of Engineering, Cardiff, United Kingdom*

Correspondence*
Joseph R. Whittaker
Whittakerj3@cardiff.ac.uk

Keywords: magnetic resonance imaging; pulsatility; cerebral arteries; echo-planar imaging; arterial stiffness; inflow effect; cerebral blood flow velocity

Highlights:

- We present a novel method for measuring pulsatility of cerebral arteries.
- The inflow effect on fast GRE imaging can be exploited to yield a flow velocity dependent signal.
- We measure pulsatile flow through cerebral arteries dynamically on a beat-to-beat basis.
- We use physiological challenges to demonstrate sensitivity to dynamic and steady-state changes in vascular tone.

Abstract

Poor arterial health is increasingly recognised as an independent risk factor for cerebrovascular disease, however there remain relatively few reliable methods for assessing the function and health of cerebral arteries. In this study, we outline a new MRI approach to measuring pulsatile flow in cerebral arteries that is based on the inflow phenomenon associated with fast gradient-recalled-echo acquisitions. Unlike traditional phase-contrast techniques, this new method, which we dub **D**ynamic **I**nflow **MA**gnitude **C**ontrast (**DIMAC**), does not require velocity-encoding gradients as

sensitivity to flow velocity results purely from the inflow effect. We achieved this desired effect using a highly accelerated single slice EPI acquisition with very short TR (15 ms) and a 90º flip angle, thus maximising inflow contrast. Simulating the spoiled GRE signal in the presence of large arteries and perform a sensitivity analysis to demonstrate that in the regime of high inflow contrast it shows much greater sensitivity to flow velocity over blood volume changes. We support this theoretical prediction with *in-vivo* data collected in two separate experiments designed to demonstrate the utility of the DIMAC signal contrast. We perform a hypercapnia challenge experiment in order to experimentally modulate arterial tone within subjects, and thus modulate the arterial pulsatile flow waveform. We also perform a thigh-cuff release challenge, designed to induce a transient drop in blood pressure, and demonstrate that the continuous DIMAC signal captures the complex transient change in the pulsatile and non-pulsatile components of flow. In summary, this study proposes a new role for a well established source of MR image contrast, and demonstrate its potential for measuring both steady-state and dynamic changes in arterial tone.

1. Introduction

Blood flow through large arteries is, due to the action of the heart, pulsatile in nature. However, elasticity of the arterial wall results in a dampening of this pulsatility, leading to steady and continuous flow in the microcirculation. This buffering effect of large arteries serves to protect the capillary bed from damage due to excessive pulsatile energy. Increased arterial stiffness, i.e. loss of elasticity, is a naturally occurring process that is mediated by numerous stressors, including mechanical factors, structural changes and atherosclerosis (Lakatta and Levy, 2003). It is primarily associated with advanced age, but is also intrinsically linked to primary hypertension (Verwoert et al., 2014), and is known to be an independent risk factor for cardiovascular disease (Mitchell et al., 2010; Wilkinson et al., 2015). As compliant (elastic) arteries act as buffers absorbing pulsatile energy generated by the heart, this stiffening is thought to have the deleterious effect of allowing pulsatile energy to propagate down to the microcirculation. Additionally, over a longer time scale increased shear stress at the endothelial surface stimulates vascular remodelling,

which is thought to have the maladaptive consequence of reducing both basal flow and vascular reactivity (Shirwany and Zou, 2010). As a very highly perfused organ, the human brain is particularly susceptible to the detrimental effects of poor arterial health, and so it is unsurprising that there is now mounting evidence to suggest a causal link between arterial stiffness and cerebrovascular disease (Hughes et al., 2018; Laurent et al., 2003; Poels et al., 2007; Poels et al., 2012). Furthermore, this emerging evidence suggests AS plays an independent role in the pathogenesis of dementia and cognitive impairment with ageing (Rabkin, 2012).

Observations over time of cerebral artery intraluminal pressure, cerebral blood volume (CBV) and cerebral blood flow velocity (CBFV) show fluctuations that span multiple temporal scales. As the cardiac cycle generates periodic pressure waves, at the high frequency end of this spectrum CBV and CBFV are characterized as being pulsatile, with a time period that fluctuates with beat-to-beat changes in heart rate variability. Direct monitoring of intraluminal blood pressure is inherently invasive, but there are several ways to noninvasively measure both CBV and CBFV, and analysis of the pulsatile component of these can be used to infer properties of the arterial vasculature, including arterial compliance. Transcranial Doppler (TCD) ultrasound measures CBFV in large cerebral arteries with sufficient temporal resolution to resolve its pulsatile component, from which an assessment of compliance can be made, either by modelling pulsatile CBV (Kim et al., 2009), or by analysis of the pulsatile component of the CBFV waveform itself (Fluck et al., 2014). The ability to measure arterial flow pulsatility is a major advantage of TCD, and simple metrics such as the Gosling pulsatility index (PI) provide a crude approximation as to the degree of pulsatile pressure entering the cranium (Naqvi et al., 2013). However, TCD has the disadvantage of being limited in sensitivity to only a few large intracranial arteries, with the proviso that a suitable acoustic window be present in the cranium at the region of interest. The lack of sensitivity to CBFV in more distal branches of the large cerebral arterial vasculature prevents direct inference of downstream stiffness, and thus makes it challenging to gauge how pulsatile pressure propagates downstream and predict where the microvasculature is most at risk.

There are numerous magnetic resonance imaging (MRI) methods that are sensitive to either CBV or CBFV, and which have been used to estimate compliance of

cerebral arteries. Arterial Spin Labelling (ASL) methods have been used to estimate compliance (Warnert et al., 2015; Yan et al., 2016), but direct measurement of arterial CBV is not trivial, and existing methods invariably suffer from low SNR. Phase contrast (PC) based MRI methods yield quantitative estimates of CBFV, and cardiac gating techniques can be used to resolve the pulsatile component of flow, from which compliance estimates can be made, e.g. via a surrogate PI metric similarly to TCD (Berman et al., 2015). PC MRI has fundamentally limited temporal resolution due to the necessity of velocity encoding gradients (VENC) to effect CBFV sensitivity, and despite advances in acquisition and reconstruction for 4D flow methods (Berman et al., 2015; Rivera-Rivera et al., 2017), these still yield only single time averaged pulsatile waveforms. One major benefit of MRI compared with TCD is its potential for a wide whole-brain field-of-view (FOV) and sensitivity to flow at multiple spatial scales, and to this end there has been a growing trend towards adapting functional MRI (fMRI) methods for spatially mapping pulsatility in the brain (Atwi et al., 2020; Bianciardi et al., 2016; Tong and Frederick, 2012; Viessmann et al., 2017). Although easy to implement and widely available, the fMRI signal is a complex mixture of multiple different physiological factors and is confounded by numerous non-flow related dynamic phenomena such as physiological motion and magnetic susceptibility effects.

Here we outline a new approach to measuring dynamic pulsatile flow through arteries, which is based on the dynamic effect of the inflow phenomenon on the magnitude of the spoiled gradient-recalled-echo (GRE) MRI signal, here termed **D**ynamic **I**nflow **MA**gnitude **C**ontrast (**DIMAC**). The purpose of this study is to reconsider a well-established source of image contrast, namely flow related enhancement, and explore how it may be utilised to measure arterial pulsatile flow dynamically, on a continuous beat-to-beat basis. To this end, we outline a theoretical motivation using simulations and a sensitivity analysis, and then follow this up with *in-vivo* demonstrations in which physiology is manipulated.

2. Methods

2.1. Theory

2.1.1. Inflow effect

The inflow phenomenon, also called time-of-flight (TOF) effect, is fundamental to the nuclear magnetic resonance (NMR) method. Even before the advent of MRI, it had been shown that the apparent longitudinal magnetisation relaxation time T_1 of flowing spin is shorter than stationary ones (Suryan, 1951). This phenomenon is exploited in order to visualize vascular networks in the form of TOF angiography, which is used clinically in the diagnosis of cerebral and coronary vascular abnormalities (Hartung et al., 2011). The mechanism behind the effect is partial saturation of the longitudinal magnetisation of stationary spins due to continual short interval RF excitation (i.e. short repetition time (TR)). In contrast, spins flowing into the imaging plane/slab do not experience this saturation effect to the same degree and so produce a stronger signal. In the extreme case of very high flow velocities (or thin slices), spins are completely refreshed between RF pulses, and so the fully relaxed equilibrium magnetisation is available to be measure in the transverse plane. In the more general case, assuming transverse magnetisation is spoiled after readout, different spin isochromats reach different steady states of longitudinal magnetisation determined by their flow velocity.

The literature already includes detailed quantitative analysis of the short TR spoiled GRE MRI signal steady state (Brown et al., 2014), including the effect of flow velocity in non-static spins (Bianciardi et al., 2016; Gao et al., 1988). In the simplest case in which a slice of thickness L is orientated perpendicularly to a blood vessel, which can be modelled as a cylinder, assuming plug flow and a 90º flip angle, the longitudinal magnetisation scales linearly with velocity v and is given by

$$M_z = M_0\left(1 - e^{\frac{-TR}{T_1}} + e^{\frac{-TR}{T_1}}\frac{v}{v_c}\right) \qquad 0 < v < v_c$$

$$M_z = M_0 \qquad v_c \geq v$$

Equation 1

where M_0 is the equilibrium magnetisation, and v_c is the critical velocity, above which the flowing spins experience only one RF pulse when crossing the excited slice. The measured signal is simply scaled by the spin density/volume and a transverse relaxation factor. The critical velocity v_c is determined by the ratio of slice thickness and TR (L/TR). If $v > v_c$ there is no longer flow dependence, and the longitudinal magnetization remains at equilibrium, in the steady state. Based on this theory, if $v < v_c$ we hypothesise that fast spoiled GRE sequences may prove very useful for measuring pulsatile flow in arteries with high temporal resolution.

2.1.2. Sensitivity analysis - simulations

The cardiac induced pressure waveform that propagates through the vasculature consequently leads to pulsatile flow in arteries (Wagshul et al., 2011), which manifests as pulsatile changes in both CBV and CBFV. In this section, we perform simulations to assess the sensitivity of the spoiled GRE signal to pulsatile changes in CBFV and CBV. The cardiac phase (τ) dependent signal can be modelled simply as the sum of intraluminal (i) and extraluminal (e) compartments

$$M_{xy}(\tau) = M_{z,i}\big(CBFV(\tau)\big) \cdot \rho_i \cdot v_i(\tau) \cdot e^{-R^*_{2,i}TE} + M_{z,e} \cdot \rho_e \cdot \big(1 - v_i(\tau)\big) \cdot e^{-R^*_{2,e}TE}$$

Equation 2

where M_z is the longitudinal magnetization defined in equation 1 (which is a function of CBFV for intraluminal spins), ρ is the spin density for the respective compartments, and v_i is the intraluminal volume (i.e. CBV). Cardiac pulsatile physiology dictates that both CBV and CBFV are functions of τ, and so too is the measured signal. The maxima of CBFV and CBV occur during the systolic peak (sys) of the cardiac phase, with baseline values observed during the diastolic (dia) portion. If during baseline a voxel is entirely contained with the vessel lumen (i.e. $v_i(\tau_{dia}) = 1$), then the measured signal will be sensitive only to changes in CBFV over the cardiac cycle. Thus, the signal is only sensitive to pulsatile CBV in voxels with an extraluminal partial volume (i.e. $v_i(\tau_{dia}) < 1$), and the degree to which depends on both the baseline partial volume and the maximum partial volume (i.e. systolic peak).

We simulate the conditions for a single voxel (with dimensions 2x2x10 mm) orientated perpendicularly to the middle cerebral artery (MCA), which we model as a straight cylinder. All MR simulation parameters are listed in Table 1. MCA CBFV varies both with cardiac cycle (i.e. pulsatility), but also across the vessel lumen due to the laminar flow profile, being strictly 0 at the vessel wall, and peaking during systole at the centre. Thus, CBFV was allowed to vary in the range between 0 – 100 cm s^{-1} to provide a realistic distribution of flow velocities (O'Rourke et al., 2020). Measuring *in-vivo* diameter changes within intracranial arteries is challenging, but high-resolution images obtained with ultra-high field MR provide the best estimates. Using this technique, it has been estimated that the MCA changes in cross sectional area by ~2.5% over the cardiac cycle (Warnert et al., 2016). Assuming a perfect cylinder this translates to a change in CBV of the same magnitude. For simulations, we assumed that CBV could increase by up to 5% of its baseline *diastolic* value. Using the above physiological ranges we assess the global sensitivity of the DIMAC signal to changes in CBFV and CBV as follows;

1. We define baseline CBFV and CBV values and calculate the signal magnitude (S).
2. We then randomly sample (1000 samples) ΔCBFV and ΔCBV values uniformly from the physiological plausible range and calculate the change in signal from baseline (ΔS).
3. We then regress ΔS against ΔCBFV and ΔCBV (normalized between 0 and 1) to estimate regression coefficients that are in units of ΔS per dynamic range of CBFV and CBV.
4. The ratio of the regression coefficients (ΔS/ΔCBFV divided by ΔS/ΔCBV) expresses the relative sensitivity to pulsatile changes in CBFV over CBV.

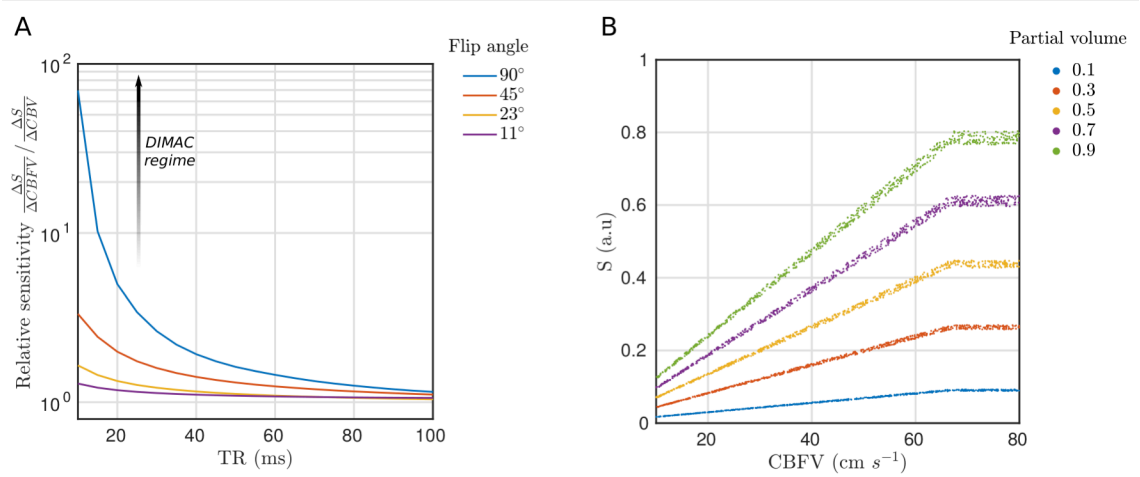

Figure 1: A) Relative sensitivity of spoiled GRE signal to pulsatile CBFV compared with pulsatile CBV, where each line represents a different flip angle. The annotated arrow represents how the GRE signal moves into the DIMAC regime of high sensitivity to pulsatile CBFV over pulsatile CBV as TR decreases and flip angle increases. B) Simulated spoiled GRE signal in the DIMAC regime of low TR (15 ms) and high flip angle (90º). Note that signal variance due to pulsatile CBV is small compared with variance due to CBFV within the normal physiological range. In every case the signal plateaus at the critical velocity 66 cm s-1, i.e. when flow velocity increases to the point when spins only experience a single RF pulse and the signal becomes sensitive to CBV alone.

Parameter	Value	Reference	Comment
Arterial blood T_1	1664 ms	(Lu et al., 2004)	At Hct = 0.42
Arterial blood T_2*	48.4 ms	(Zhao et al., 2007)	At sO_2=98% and Hct = 0.44
CSF T_1	3817 ms	(Lu et al., 2005)	
CSF T_2*	400 ms	(Pinto et al., 2020)	
Arterial blood ρ	0.85	(Herscovitch and Raichle, 1985)	Assume Hct = 0.44
CSF ρ	1		Assume like water

Table 1: MR parameters for simulation at 3T.

Fig.1A shows the relative sensitivity of the GRE MRI signal as a function of TR for different flip angles. The sensitivity to CBFV increases rapidly as TR is decreased, and this is most pronounced for the maximum α=90º. Thus, we define the "DIMAC regime" as this region of the GRE parameter space that engenders high sensitivity to

pulsatile CBFV. Fig.1B shows the simulated signal plotted as a function of CBFV in the case of α=90º and TR=15 ms, where it can be clearly seen that the effect of pulsatile CBV is very small compared to CBFV when $v < v_c$, which in this simulation is 66cm/s. When $v > v_c$, all flow sensitivity is lost and the signal is purely sensitive to changes in CBV, although at a much reduced dynamic range. It is also evident that the two parameters are coupled so that the dynamic range of CBV signal variance scales with CBFV, and that the magnitude of the signal is dependent on baseline partial volume. These results suggest that in the DIMAC regime of high saturation (TR=15ms, flip=90°), partial volume of arterial blood merely scales the overall signal magnitude, which is always relatively more sensitive to pulsatile CBFV over CBV. This is clearly also a reflection of the physiology of large cerebral arteries, i.e. they have high CBFV, but are relatively stiff and thus only exhibit small pulsatile CBV.

2.1.3 Impact of SNR

We simulated different levels of SNR to explore how the predictions of the sensitivity analysis would translate to the *in-vivo* scenario. The beat-to-beat pulsatile CBFV is modelled with a Fourier basis set as

$$CBFV(\tau) = CBFV_{dia} + \sum_{n=1}^{N} c_n \cdot e^{i\frac{2\pi n\tau}{P}}$$

Equation 3

where $CBFV_{dia}$ is the baseline (i.e. dc component) during diastole, P is the beat-to-beat time period, and n is the harmonic of the fundamental frequency. A total of $N = 10$ harmonics were used taken from (Yang et al., 2019) in order to model a generic pulsatile flow response. The pulsatile signal was then modelled for different baseline partial volumes and SNR levels. As seen in Fig.2A the quality of the CBFV weighted pulsatile signal is a function of both baseline partial volume and SNR, which determines the fidelity with which single beats can be resolved. Fig.2B plots the agreement of the simulated signal with the pulsatile CBFV waveform, and it can be seem that even in the lowest partial volume and SNR case, although individual beats can't be seen, with sufficient averaging (100 beats) the MR signal still shares more than 50% variance with the pulsatile CBFV. In cases of high SNR and baseline

partial volume, easily achievable *in-vivo*, the individual beats can be resolved with high fidelity.

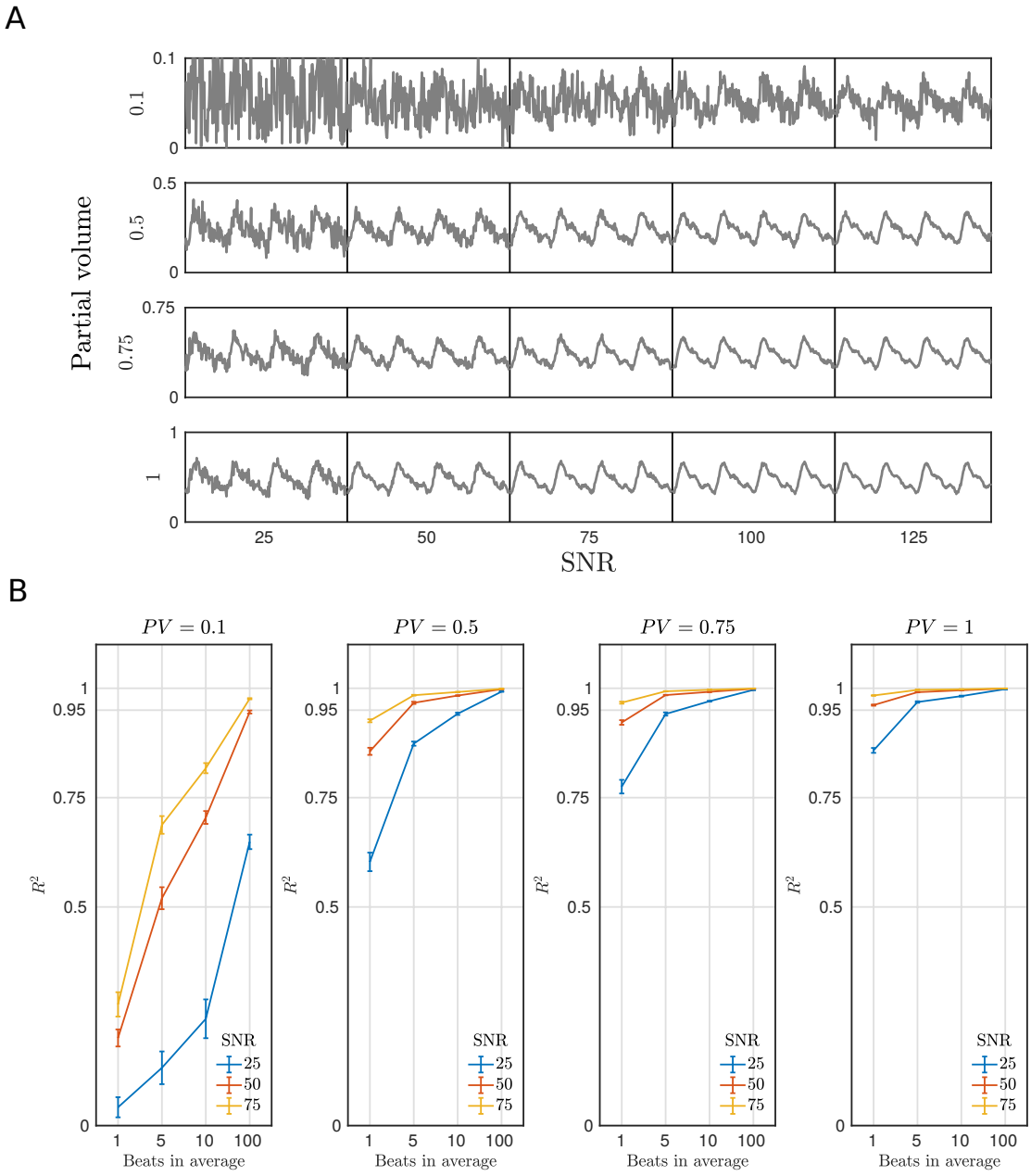

Figure 2: A) Simulated DIMAC signal over 4 beats. Each panel represents a different partial volume (row) and SNR condition (column). Note the different y-axis scale for each partial volume. Thus, for a given SNR, increased partial volume of arterial blood increases signal magnitude and yields a stronger pulsatile signal. B) Each panel shows the amount of variance explained in the true CBFV waveform by the simulated DIMAC signal as a function of number of beats included in the average. Naturally, as the number of beats included in the average increases more noise is averaged out, and thus the R^2 increases. However this also shows that when both partial volume and SNR are sufficiently high, individual beats can be resolved with high fidelity (i.e. a high R^2 with respect to the true CBFV waveform).

2.2. Experimental Protocol

We performed two separate *in-vivo* MRI experiments using a highly accelerated GRE echo-planar-imaging (EPI) acquisition to demonstrate the potential of the DIMAC method as follows: i) an experiment to estimate the steady-state cardiac induced pulsatile flow response in the middle cerebral artery (MCA), using a hypercapnia challenge to demonstrate the sensitivity of DIMAC to subtle changes in vascular tone (*HC-challenge* experiment); ii) a dynamic experiment during a thigh cuff release (TCR) challenge to demonstrate sensitivity to dynamic changes in the non-pulsatile component of CBFV, and beat-to-beat pulsatile flow velocity (*TCR-challenge* experiment). Finally, we also performed a simple flow phantom experiment with the same acquisition in order to verify the strong flow velocity dependent signal that is predicted in the very short TR domain (included in *Supplementary material*).

2.2.2. Imaging protocol

All experiments described below were performed on a Siemens 3T MAGNETOM Prisma clinical scanner with a 32-channel receiver head-coil (Siemens Healthcare GmbH, Erlangen), and used a prototype single slice GRE EPI sequence, with the number of repetitions varied according to the experimental requirements (see following sections). The protocol was optimized for maximum sensitivity to the inflow effect by making the TR as short as possible. This included removing fat saturation pulses and using ramp sampling. Acquisition parameters were as follows: flip angle=90º, FOV=192mm (2 mm^2 in-plane resolution), GRAPPA=5, partial Fourier = 6/8, TR=15ms, TE=6.8ms, slice thickness=10mm. For all in-vivo experiments standard TOF scans were performed in order to guide the placement of DIMAC slices perpendicularly to the artery of interest. All participants gave written informed consent, and the School of Psychology Cardiff University Ethics Committee approved the study in accordance with the guidelines stated in the Cardiff University Research Framework (version 4.0, 2010). Data are publically available through the Open Science Framework (DOI 10.17605/OSF.IO/ZQ5E3).

2.2.3. In-vivo experiments

2.2.3.1. HC-challenge experiment

An experiment was performed in 5 healthy participants to demonstrate the sensitivity of DIMAC to measuring arterial pulsatility in-vivo. A hypercapnia challenge (HC) in which two distinct levels of partial pressure of end-tidal CO_2 ($P_{ET}CO_2$) were targeted was used as a global vasodilatory stimulus in order to model subtle changes in vascular tone.

For each subject a series of scans was performed, which included acquisitions with the default protocol (TR = 15 ms, 4096 repetitions), and 3 modified acquisitions in which the TR was increased by a factor of 2 (i.e. TR = 30,60, and 120 ms). For the modified acquisitions the number of repetitions was adjusted likewise by a factor of 2 (i.e. 2048, 1024, and 596 repetitions), such that the scan length was always exactly 61.44 seconds. In addition to modifying TR, scans were also performed at 3 distinct levels of $P_{ET}CO_2$, in which levels were defined with respect to individual subject baseline levels, which were determined during the initial set up period during the experiment. For each TR protocol, acquisitions were repeated at normocapnia (+0 mm Hg w.r.t. baseline), and two levels of hypercapnia (+4 and +8 mm Hg w.r.t. baseline). Thus, for each subject a series of twelve scans in total was performed, i.e. each of the 4 TR protocols at each of the 3 hyerpcapnia levels. The experiment therefore had a factorial design with 2 factors (TR and HC) with 4 and 3 levels respectively (TR15, TR30, TR60, and TR120; HC0, HC4, and HC8). For each HC level the order of scans was the same (TR15, TR30, TR60, TR120), but the order of HC levels was randomised across subjects.

The details of the HC experiment are as follows. A tight fitting mask was used to manually deliver gas through a system of custom-made flow meters, as previously described (Whittaker et al., 2016). A sampling line connected to the mask was used to monitor $P_{ET}CO_2$ levels, and flow of medical air and 5% CO_2 was manually adjusted to target discrete levels (+4 and +8 mm Hg) above the participant's predetermined baseline value. The baseline level was determined on an individual subject bases at the beginning of each scanning session. The mask circuit setup allowed gases to mix in a length of tubing before reaching the mask, and a minimum total flow rate of 30 L/min was maintained at all times. For the normocapnia scans only medical air was delivered. For hypercapnia scans the flow rates were adjusted

to achieve the desired target prior to the start of the acquisition, with sufficient time given to ensure a steady state was reached. Flow was always returned to medical air in between HC levels to allow subjects to return to baseline, and subjects were given ~1-2 min of recovery at baseline between hypercapnia levels. The start of a new hypercapnia level and delivery of CO_2 gas was always preceded with the subject's verbal consent. For each hypercapnia period, at least 1 minute was allowed when transitioning to a new $P_{ET}CO_2$ level in order to ensure a steady state at the target end-tidal value was reached. As there were different TR protocols for each HC level, each lasting ~1 min, when factoring in transitions, subjects were only ever at a particular hypercapnic level for ~5-10 min. Fig.2 in the *Supplementary material* shows an example PETCO2 trace and relative scan timings for one subject. All subjects tolerated the HC challenge well and none reported and significant discomfort. Additionally, photoplethysmography (PPG) traces were recorded concurrently to provide an independent measure of the cardiac cycle.

2.2.3.2 TCR-challenge experiment

An experiment was performed in a single subject to demonstrate the utility of DIMAC for measuring changes in flow/pulsatility dynamically. In order to modulate flow we used a thigh cuff release (TCR) challenge, as it is known to cause a robust transient drop in blood pressure (Aaslid et al., 1989; Mahony et al., 2000). A single transverse slice was placed in the neck at a position approximately perpendicular to both the internal carotid arteries (ICA) and vertebral arteries (VA), as shown in Fig. 3C. The TCR protocol, detailed here in conference abstract form (Whittaker et al., 2020), was briefly as follows: Pneumatic cuffs were placed around the tops of both thighs and inflated to +40 mm Hg above baseline systolic BP pressure for 152 s and then rapidly deflated. Scanning of the DIMAC acquisition was timed such that data collection began 20 s before deflation, and each scan lasted ~60s (4096 repetitions). A series of 5 TCR manoeuvres were repeated, and both concurrent PPG and beat-to-beat blood pressure (Caretaker, Biopac) traces were recorded.

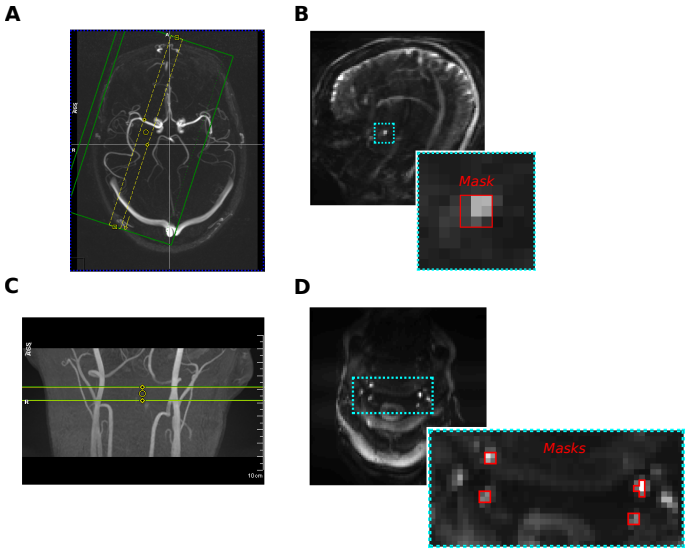

Figure 3: A) An example of the slice placement at the M1 segment of the MCA for the *HC-challenge* experiment. B) An example DIMAC image, including MCA mask. C) Slice placement for the subject in the *TCR-challenge* experiment placed to include best perpendicular placement of bilateral ICAs and VAs. D) Subject's DIMAC EPI image and artery masks.

2.3. Analysis

2.3.2. In-vivo experiments

Data for both in-vivo experiments were processed using AFNI (Cox, 1996) and MATLAB. All images were first motion corrected using AFNI's 2dImReg function and filtered to remove linear drifts. Subsequent analysis of the data was performed on ROI average time series and is described below. For the TR15 condition, pulsatile CBFV weighting in the signal is sufficiently high such that the periodic signal is clearly visible and we could perform peak detection to identify each cardiac cycle without the need for the external PPG, which we refer to as *Beat-to-beat fit* and describe below. For the other TR conditions this peak detection is no longer possible, but the pulsatile component of the signal can still be extracted by using the PPG as an external reference of the cardiac phase, which we refer to as *Cardiac binned average*, and describe below. However, with this method, only a time average pulsatile component can be extracted.

2.3.2.1. Cardiac binned average

As has been previously done with PC and fMRI approaches, we can use the PPG as an external reference to determine in which phase of the cardiac cycle a particular MR image was acquired. *Systolic* peaks were detected in the PPG signal, and then each beat-to-beat interval was split into a set of *n* cardiac bins. Thus, individual data points in the time series could be sorted into one of these *n* bins, and then averaged into a new *n* point cardiac phase time series, representing the time averaged pulsatile component of the signal. As the sampling rate is different for each TR protocol, the number of bins *n* was varied to be approximately half the sampling rate, according to equation 4.

$$n = \left\lceil \frac{1}{2TR} \right\rceil$$

where $\lceil x \rceil$ is the ceiling function that rounds x up to the next integer value. With this method we also calculated a time averaged pulsatility index (PI), a simple metric for quantifying the degree of pulsatility in the signal, and defined as the maximum value of the average signal minus the minimum value divided by the mean.

2.3.2.2. Beat-to-beat fit

As is customary with pulsatile flow waveforms, a Fourier series basis set was used to model the pulsatile component of the signal. In order the detect this on an individual beat-to-beat basis the *diastolic* peak of each cardiac cycle was detected (see Fig. 4B), and then, after removal of linear trends, linear regression was used to fit Fourier basis set to the signal between each pair of *diastolic* peaks. Fig. 4A shows the average R^2 of individual beat-to-beat fits for the *HC-challenge* experiment (averaged across HC condition and subject for the TR15 condition only). As expected the R^2 increases with the number of harmonics included in the Fourier basis set and begins to plateau at 6. Thus, 5 terms (the fundamental frequency + 4 higher order harmonics) was chosen as the best balance between goodness-of-fit and parsimony, as increasing to a greater number of terms offers only marginal increases in R^2, but at the risk of over-fitting. As each individual beat is characterised by its own set of Fourier coefficients, the time averaged pulsatile waveform can be modelled by simply averaging these together, and then estimated with an arbitrary number of data points.

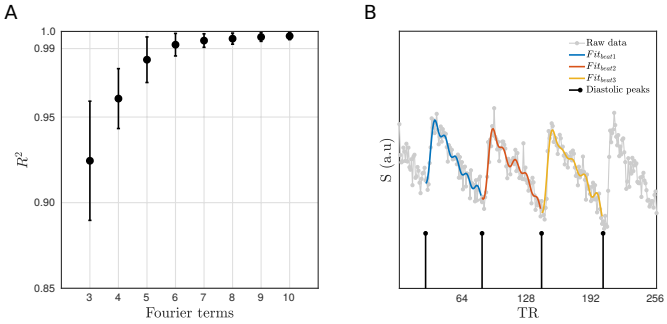

Figure 4: A) The average amount of variance explained in the beat-to-beat fit as a function of the number of Fourier terms used. B) An example showing detected *diastolic* peaks and the beat-to-beat pulsatile fits.

Additionally, *systolic* peaks (i.e. maximum signal during systole) were also detected. Both *diastolic* and *systolic* peaks were up-sampled to the original sampling frequency to create *diastolic* and *systolic* time series respectively. Thus, the whole time series could be deconstructed into a non-pulsatile component (i.e. the low frequency fluctuating *diastolic* peaks), and individual beat-to-beat pulsatile components that could be characterised by a set of Fourier coefficients. The *diastolic* and *systolic* time series are equivalent to the envelop of the dynamic pulsatile signal and contain low frequency information related to the physiological factors that affect the non-pulsatile component of CBFV.

2.3.2.3. HC-challenge experiment

For each subject, ROIs located at the MCA were defined from the average image across all scans, as a 9 voxel mask encompassing the artery, which was selected manually such that the centre voxel was the brightest in the region of the artery (see Fig.1B). For the default protocol (TR15), each ROI time series was processed using the *Beat-to-beat fit* method described above. Fourier coefficients for each individual beat were averaged together and then the time-averaged waveform was reconstructed with 100 data points. Additionally, the ROI time series were also processed using the *Cardiac binned* average method in order to calculate and compare the PI across all TR conditions. The PI was calculated for each TR and HC condition, and then a repeated-measures ANOVA was used to test for an effect of TR on PI, after averaging across HC levels.

2.3.2.2. TCR-challenge experiment

For each subject 4 ROIs were created encompassing the ICAs and VAs bilaterally as follows; the brightest voxel in the region of each artery was used to define the centre of a 5x5 voxel search space, within which the 4 brightest voxels were selected to form a mask. As shown in Fig.1.D, voxels in all masks were contiguous to create a single ROI for each artery. Average time-series were extracted from each ROI and then processed using the *Beat-to-beat fit* method described above.

3. Results

3.1. In-vivo experiments

3.1.2. HC-challenge experiment

The theory predicts that in the “DIMAC regime” there is a strong sensitivity to pulsatile CBFV, and comparing the signal from the different TR conditions empirically supports this. A strongly periodic pulsatile signal is evident in the time series for the TR15 condition, but is far less visible for the TR30 condition, and not readily visible for the TR60 and TR120 conditions (see Fig 5A), as predicted by the theory. This is also reflected in the power spectra, with the power of the fundamental cardiac frequency clearly reducing as a function of TR, and higher order harmonics becoming less well defined also (see Fig 5A). Fig 5B shows the PI for each TR and HC condition. It is clear, as expected, that the PI is strongly dependent on TR condition, and this is quantitatively verified by the results of a repeated measures ANOVA on PI, which shows a significant effect of TR ($p=0.00062$).

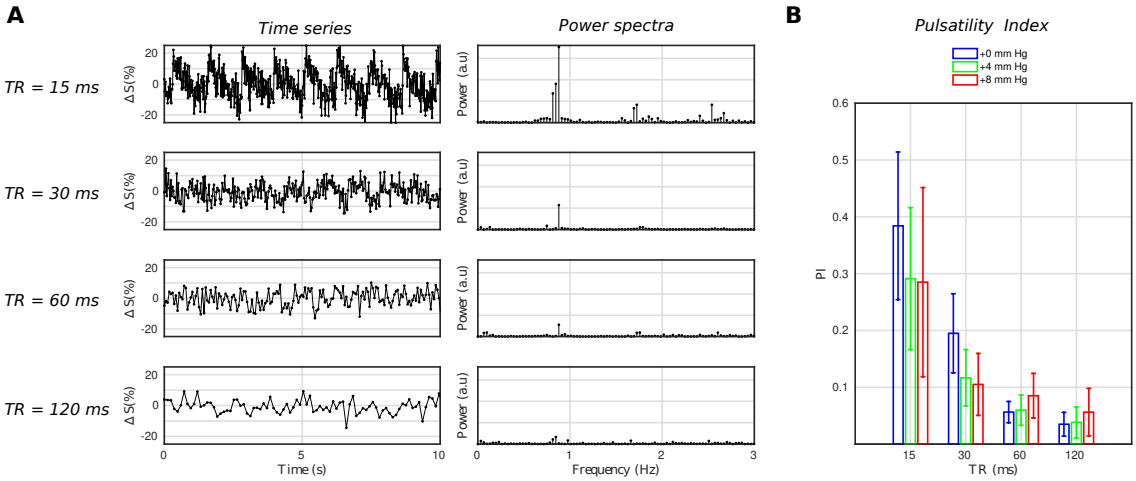

Figure 5: A) Example (subject 1) time series and their power spectra for each TR condition. Both the time series and power spectrum make it clear that there is a strong degree of pulsatility for the TR15 conditions, which falls away with higher TR values as predicted by the theory. B) The pulsatility index for each TR and HC condition, which quantitatively confirms that which is observed in A.

Figure 6A shows the first 15 s of the DIMAC time series for each subject in the HC0 condition, along with the beat-to-beat fit. Qualitatively one can observe differences in the pulsatile signal shape across subjects, which is more clearly seen in the average responses for each subject in Fig. 6B. One can also see in Fig. 6A that there is beat-to-beat variability in the pulsatile signal, for example in the subject presented in the fifth row, one can see that the first few beats are qualitatively different in shape to the later beats.

Fig. 6C shows the group average cardiac phase waveforms across different HC conditions. The cardiac phase waveforms show at least two clear peaks, which are consistent with what is observed with TCD (Kurji et al., 2006; Robertson et al., 2008), with the first one representing the systolic peak, and the second one representing a reflection wave, preceded by the so called “Dicrotic notch”, related to a transient increase in pressure associated with the aortic valve closing. Qualitatively there is a clear modulation of the waveform baseline with increasing levels of hypercapnia, due to increased flow velocity, and also clear modulation of the waveform shape. With increased hypercapnia the two peaks become broader, and less clearly separated from one another. There is also evidence of an additional reflection peak appearing on the downward slope of the primary peak, which becomes more pronounced with increasing hypercapnia and has previously been demonstrated with TCD (Robertson

et al., 2008). Closer peaks may indicate resonance effects produced by pressure waves in shorter vascular systems (Nichols et al., 2011).

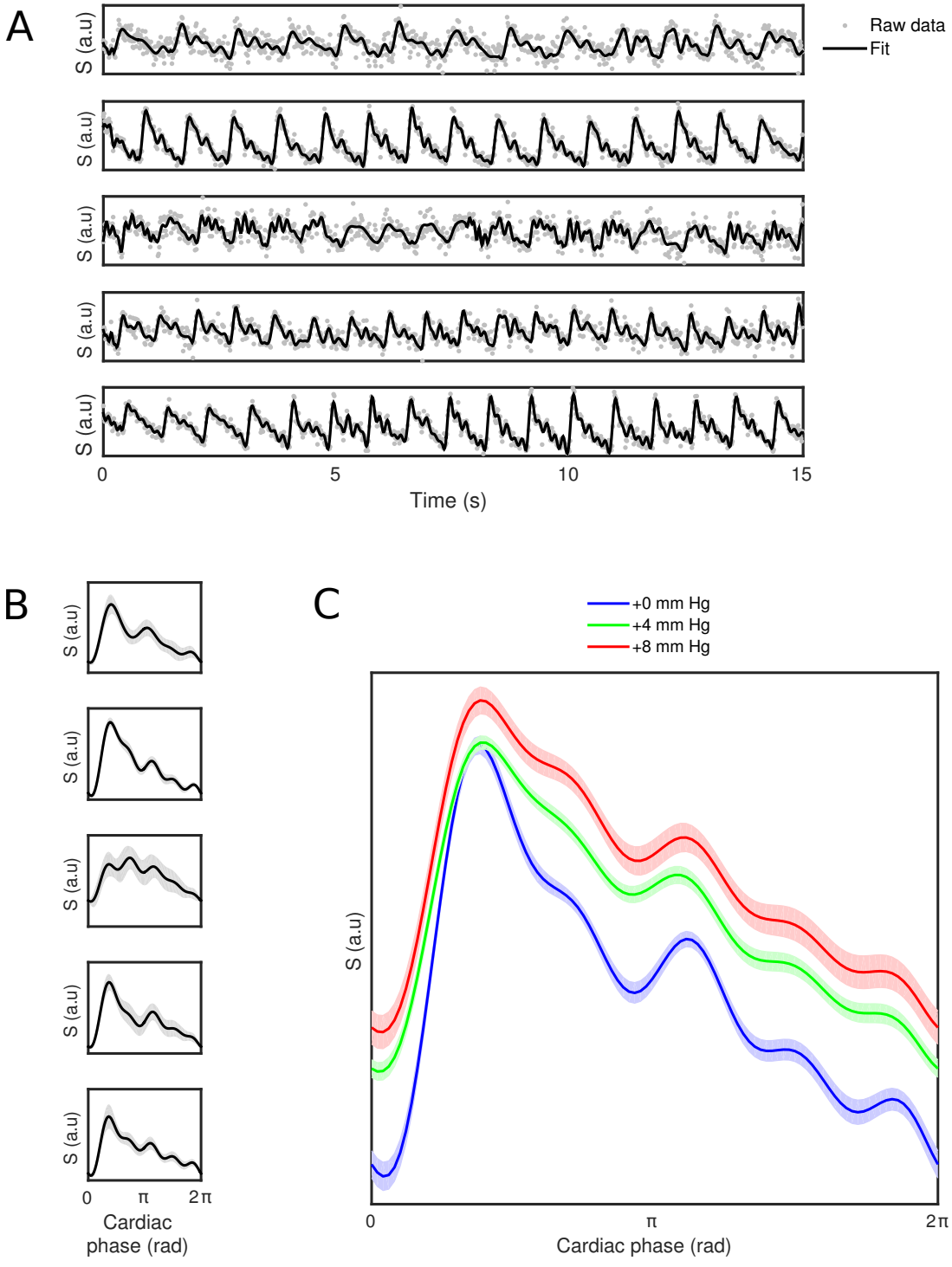

Figure 6: A) First 15s of time series for each subject for HC-challenge data (TR15 and HC0 condition), with beat-to-beat fit overlaid. B) The mean pulsatile waveform (±SD shaded area) for each subject (TR15 and HC0 condition). C) The across subject mean pulsatile waveforms ((±within subject error shaded area)

for each HC condition of the HC-challenge. Qualitatively one can see the pulsatile waveform shape is modulated by hypercapnia.

3.2.2. TCR-challenge experiment

Fig. 7A shows the first 15 seconds of the L-ICA DIMAC signal along with the beat-to-beat fit and the signal *diastolic* and *systolic* peaks. A very strong periodic signal is clearly observable, with the prominent systolic and wave reflection peaks discernable on a beat-to-beat basis. Figure 5B shows the full *systolic* and *diastolic* peak time courses of the signal during the thigh cuff release challenge in both left and right ICA and VAs. The magnitude of the signal changes are larger in the ICAs than in the VAs, and the traces appear smoother, which is perhaps not surprising given that the ICAs are larger arteries (diameter of ~5 mm compared with ~3 mm for VA), and thus will have higher SNR. The event-locked change in the CBFV evoked by the TCR is present in the signal *systolic* and *diastolic* peak time courses, and is clearly seen bilaterally in the ICA, but only partially in the VA, primarily in the left branch. Interestingly, it is also clear that the TCR response in the ICA *systolic* peak time series is delayed with respect to the *diastolic* peak time series. Furthermore, the *diastolic* peak response shows a marked drop in amplitude, followed by a subsequent overshoot, whereas the *systolic* peak response shows a simple slowly evolving increase in amplitude and return to baseline. *Supplementary material* Fig.3 examines the TCR response more closely in the ICA DIMAC *systolic* and *diastolic* peak time series and compares them with the heart rate and mean arterial blood pressure responses, which demonstrates that these DIMAC signal changes are clearly of a physiological origin.

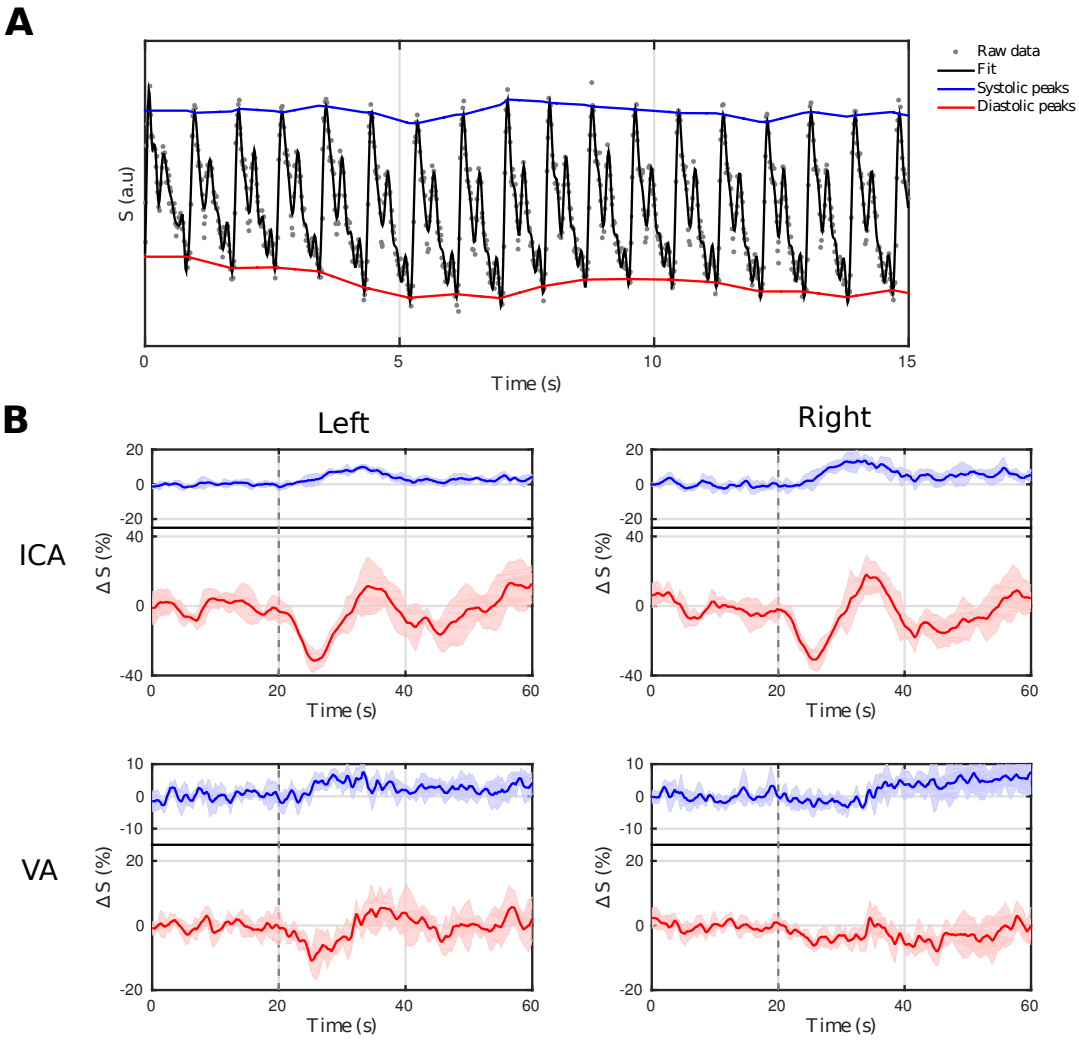

Figure 7: A) First 15s of the *TCR-challenge* time series taken from the left ICA ROI. B) The *systolic* (blue) and *diastolic* (red) peak time series (i.e. signal envelope) averaged across the five repeats, for both ICA and VA bilaterally. The onset of the thigh-cuff release is highlighted with a dotted grey line. Both left and right ICA show clear time locked responses to the *TCR-challenge* in both *systolic* and *diastolic* time series. The same responses are far less evident in the VA time series, particularly in the right side.

4. Discussion

In this paper we have proposed a new approach, which we have dubbed Dynamic Inflow Magnitude Contrast (DIMAC), for studying cerebral arterial pulsatile flow. Using a two-compartment model we simulated the spoiled GRE signal, and have shown that at short TRs and high flip angles, it is strongly sensitive to pulsatile CBFV. We propose that this DIMAC signal regime is a promising new way to measuring pulsatile arterial flow, which we support with *in-vivo* data. Bianciardi et al previously advanced the GRE MRI signal as a tool for measuring pulsatility in the

brain (Bianciardi et al., 2016). Their approach was designed to yield only sensitivity to CBV, by choosing acquisition parameters that resulted in no sensitivity to realistic blood flow velocities (i.e. a very low critical velocity v_c). However, as outlined in this study, the theory suggests that an alternative strategy may be more beneficial, particularly when focussing on large arteries. We have shown that in the "DIMAC regime" of short TR and high flip angle, when focussed on large cerebral arteries, the high sensitivity to the inflow effect in the spoiled GRE signal creates a novel CBFV dependent image contrast that allows pulsatile flow to be measured with high sensitivity. Compared to traditional techniques, the DIMAC method offers very high temporal resolution, akin to TCD, which allows the individual beat-to-beat pulsatile component of flow to be resolved, but whilst retaining the advantages of MRI. Furthermore, when considering large arteries, the physiological conditions greatly favour the DIMAC method over CBV based approaches. This is because these large arteries show only fractionally very small cardiac induced volume changes, compared with the large dynamic range seen in CBFV.

4.1. Dynamic measurements

A major advantage of the DIMAC approach we have outlined is the ability to measure pulsatile flow dynamically, and resolve individual beat-to-beat pulsatile waveforms. The current preferred MRI approach for measuring arterial pulsatility is PC-MRI, although with this method CBFV measurements are not usually made continuously, but rather are averaged over many cardiac cycles. Depending on the temporal width of the bins into which the cardiac phase is separated, this typically leads to significant morphological differences between PC-MRI and TCD CBFV waveforms (Wagshul et al., 2011), best characterised as a loss of fine structure, i.e. fewer clearly resolved distinct peaks and troughs. These key features (peaks and troughs and their relative timings) that have been used to characterise the CBFV waveform in the TCD literature (Aggarwal et al., 2008; Kurji et al., 2006; Lockhart et al., 2006; Robertson et al., 2008), are often integral to attempts to indirectly derive higher order measures of the cerebrovascular system such as intracranial pressure and cerebral perfusion pressure (Aggarwal et al., 2008), or downstream compliance (Robertson et al., 2008). In this study a simple averaging of Fourier terms was used to reduce noise and characterise pulsatility both at the subject and group level, but in

theory more complex processing strategies could be used that incorporate the non-stationary nature of the cardiac cycle, and crucially the ability to resolve individual beats permits higher level measures of variability to be obtained. Thus, the continuous measurement and beat-to-beat sensitivity of DIMAC not only allows pulsatile waveforms to be measured with higher fidelity, but also allows the inherent (and physiologically relevant) variability to be quantified.

In addition to the aforementioned benefits with regard to characterising pulsatility, the continuous measurement approach also preserves the non-pulsatile components of CBFV. This is important because arterial health is not only concerned with the passive transmission of pulsatile energy throughout the system, and thus the resulting and measurable pulsatility, but also the more active processes of CBF regulation that occurs via multitude of local, neural, metabolic and mechanical factors. Dynamic cerebral autoregulation (CA) of CBF, which is critically important for neurological health, depends on the healthy function of arteries, and evidence suggests that atherosclerotic associated changes lead to adaptive remodelling that results in both reduced basal flow (Silver and Vita, 2006) and reduced vascular reactivity (Kim et al., 2009). Thus, MRI methods such as DIMAC that, like TCD, offer high temporal resolution continuous flow measurement in which both pulsatile and non-pulsatile components are resolved, are highly desirable. We demonstrated the utility of the DIMAC method to this end by showing its sensitivity to physiological changes induced by a transient blood pressure challenge. Although we have only considered the *systolic* and *diastolic* peak time series signal, there is clearly huge scope for new pulse wave analysis approaches to be developed. New clinical tools based on MRI derived dynamic metrics of cerebral arterial function are highly desirable for conditions such as Alzheimer's disease, with which impaired CA and vasomotor function are thought to be important (Claassen and Zhang, 2011; Di Marco et al., 2015; Niwa et al., 2002; Zhou et al., 2019), but have hitherto remained relatively less well studied.

4.2. Flow velocity

The basis of the method outlined in this study is that the spoiled GRE signal becomes very sensitive to flow velocity in the DIMAC regime of short TR and high

flip angle. This fact in conjunction with the physiology of flow in large arteries makes it useful for efficiently measuring pulsatility in these arteries. One inherent limitation to this approach is the critical velocity v_c that determines the upper limit of sensitivity. Unlike the PC-MRI approach where the limits of sensitivity can be more easily manipulated by appropriately choosing the velocity encoding (VENC) parameter, with the DIMAC method, fundamental physical and hardware limitations and practical considerations effectively determine v_c. However, unlike PC-MRI where misspecification leads to aliasing of velocities that exceed the VENC, with DIMAC the signal merely saturates at velocities exceeding v_c. The parameters used here predict a v_c of ~ 67 cm s^{-1}, which is below the peak velocity one might expect to measure for ICAs, and on the limit for MCAs (Brant, 2001), which risks losing sensitivity to the most central lamina of the cross-sectional flow distribution.

Additionally, a benefit of PC-MRI is that it renders a pure CBFV contrast in the phase signal, which with careful consideration of acquisition and analysis protocols can be quantified in meaningful units. The primary purpose of this study was to demonstrate the principle of DIMAC and so in its current implementation provides a non-quantitative assessment of a predominantly CBFV weighted signal. However, in the *Supplementary material* we include the results of a flow phantom study, which shows how in principle DIMAC may be extended to yield quantitative CBFV measurements. This is achieved by acquiring a separate M_0 image (i.e. one with a sufficiently long TR such that the flowing blood only experiences a single RF pulse), which is then used to scale velocity dependent magnetisation in equation 1. The results of this simple experiment suggest that with further research efforts, quantitative CBFV estimates might be obtained. The main barrier to this in the present study is the limited spatial resolution, which will result in partial volume effects with CSF and contributions to the signal from changes in CBV (Bianciardi et al., 2016; Viessmann et al., 2017). Such partial volume effects lead to multiple sources of signal contrast that present a challenge for clinically useful interpretations of pulsatile flow waveforms (Viessmann et al., 2017). However, as demonstrated by the simulations presented in Fig.1, in the DIMAC regime the signal from static spins is effectively nulled, due to the saturating effect of a train of short interval, high flip angle RF pulses, so non-blood partial volumes only contribute marginally to the total signal variance. Still, this topic warrants further investigation, and analysis with a better

608 informed multi-compartment model, may well be a fruitful avenue for future research,
609 and prove useful for separating the effects of CBFV, CBV and CSF partial volume
610 changes. Furthermore, as the theory suggest that non-blood partial volumes will
611 reduce the overall magnitude of the signal, but not affect the sensitivity to CBFV with
612 respect to CBV (see Fig.1B), this implies that by going to high field strengths one
613 may leverage the inherent increased SNR to target smaller sub-voxel arteries.

614 Finally, the sensitivity analysis included in the theory section is based on the
615 assumption of plug flow, which cannot be assumed in the true physiological case.
616 For the purposes of making a broad statement about the signal sensitivity we don't
617 believe this to be a significant limitation, however it is something that should be
618 considered in future work. Modelling the signal with a more realistic laminar flow
619 profile may help to optimise the acquisition further as the sensitivity profile presented
620 in Fig.1A may be overly simplified. Furthermore, it may be useful for optimising the
621 acquisition for more targeted assessment of different arterial sites and scales (i.e.
622 considering smaller arteries than here), based on detailed a priori information about
623 the specific flow profile.

624 ### 4.3. Acquisition considerations

625 Single-shot EPI was chosen here because of its efficiency, which is necessary for
626 the short sampling rates required for DIMAC, however it is limited in its achievable
627 spatial resolution, and is associated with various artifacts and distortions due to the
628 overall long sampling period. Although we have shown here that the relatively poor
629 image fidelity of our EPI implementation does not present a major obstruction to the
630 overall aim of extracting high temporal resolution pulsatile flow information, that is
631 not to say that improvements in image quality or spatial resolution would not be
632 beneficial. Alternatively, this limitation may be better addressed directly by exploring
633 different sampling schemes that permit higher spatial resolutions, but still keep TR
634 short (and thus saturation of static tissues high), such as multi-shot segmented EPI.
635 Furthermore, reductions in TR become increasingly difficult without using small flip
636 angles due to SAR restrictions. As the limits of the technique are pushed, alternative
637 low SAR pulse options may also need to be considered, such as using the VERSE
638 technique (Conolly et al., 1988; Hargreaves et al., 2004).

5. Conclusion

The pulsatile nature of arterial blood flow provides a clinically relevant insight into arterial structure/function and its effect on cerebral health. In this study, we demonstrate the feasibility of a new approach to measuring pulsatile flow in cerebral arteries by exploiting the inflow effect that is present in highly accelerated GRE acquisitions. We have shown that the efficiency of this DIMAC approach allows for dynamic beat-to-beat assessment of pulsatile flow without requiring averaging across cardiac cycles. Measured responses to the thigh cuff challenge demonstrate the power of this technique to observe transient cerebrovascular processes in multiple vessels in the brain, opening up the possibility of studying blood flow dynamics and cerebral autoregulation to multiple distinct brain regions. Furthermore, we have shown that the technique is sensitive to subtle changes in physiology as demonstrated here using a hypercapnic challenge. We believe this novel DIMAC method provides a promising new approach for studying cerebral arterial function, which will ultimately be valuable in researching arterial function in ageing and cerebrovascular disorders such as dementia and small vessel disease.

6. Acknowledgments

This work was funded in whole, or in part, by the Wellcome Trust [WT200804]. For the purposes of Open Access, the author has applied a CC BY public copyright license to any Author Accepted Manuscript version arising from this submission. Thanks to Peter Weale for valuable input during pilot scanning.

7. Declaration of interest

Fabrizio Fasano and Patrick Liebig are employees of Siemens Healthcare. Joseph Whittaker, Fabrizio Fasano, Patrick Liebig, and Kevin Murphy are all named inventors on a patent (Patent No: US 10,802,100 B2. Date of Patent: Oct 13, 2020) which covers aspects of this research (Whittaker, 2019).

8. References

Aaslid, R., Lindegaard, K.F., Sorteberg, W., Nornes, H., 1989. Cerebral autoregulation dynamics in humans. Stroke 20, 45-52.

Aggarwal, S., Brooks, D.M., Kang, Y., Linden, P.K., Patzer, J.F., 2nd, 2008. Noninvasive monitoring of cerebral perfusion pressure in patients with acute liver failure using transcranial doppler ultrasonography. Liver Transpl 14, 1048-1057.

Atwi, S., Robertson, A.D., Theyers, A.E., Ramirez, J., Swartz, R.H., Marzolini, S., MacIntosh, B.J., 2020. Cardiac-Related Pulsatility in the Insula Is Directly Associated With Middle Cerebral Artery Pulsatility Index. Journal of Magnetic Resonance Imaging 51, 1454-1462.

Berman, S.E., Rivera-Rivera, L.A., Clark, L.R., Racine, A.M., Keevil, J.G., Bratzke, L.C., Carlsson, C.M., Bendlin, B.B., Rowley, H.A., Blennow, K., Zetterberg, H., Asthana, S., Turski, P., Johnson, S.C., Wieben, O., 2015. Intracranial Arterial 4D-Flow is Associated with Metrics of Brain Health and Alzheimer's Disease. Alzheimers Dement (Amst) 1, 420-428.

Bianciardi, M., Toschi, N., Polimeni, J.R., Evans, K.C., Bhat, H., Keil, B., Rosen, B.R., Boas, D.A., Wald, L.L., 2016. The pulsatility volume index: an indicator of cerebrovascular compliance based on fast magnetic resonance imaging of cardiac and respiratory pulsatility. Philos Trans A Math Phys Eng Sci 374.

Brant, W.E., 2001. The Core Curriculum: Ultrasound. Lippincott, Williams & Wilkins, Philadelphia.

Brown, R., Cheng, Y.N., Hacke, E.M., Thompson, M.R., Venkatesan, R., 2014. Magnetic Resonance Imaging: Physical Principles and Sequence Design, 2nd ed. John Wiley & Sons, Inc, New Jersey.

Claassen, J.A., Zhang, R., 2011. Cerebral autoregulation in Alzheimer's disease. J Cereb Blood Flow Metab 31, 1572-1577.

Conolly, S., Nishimura, D., Macovski, A., Glover, G., 1988. Variable-rate selective excitation. Journal of Magnetic Resonance (1969) 78, 440-458.

Cox, R.W., 1996. AFNI: software for analysis and visualization of functional magnetic resonance neuroimages. Comput Biomed Res 29, 162-173.

Di Marco, L.Y., Farkas, E., Martin, C., Venneri, A., Frangi, A.F., 2015. Is Vasomotion in Cerebral Arteries Impaired in Alzheimer's Disease? J Alzheimers Dis 46, 35-53.

Fluck, D., Beaudin, A.E., Steinback, C.D., Kumarpillai, G., Shobha, N., McCreary, C.R., Peca, S., Smith, E.E., Poulin, M.J., 2014. Effects of aging on the association between cerebrovascular responses to visual stimulation, hypercapnia and arterial stiffness. Front Physiol 5, 49.

Gao, J.H., Holland, S.K., Gore, J.C., 1988. Nuclear magnetic resonance signal from flowing nuclei in rapid imaging using gradient echoes. Med Phys 15, 809-814.

Hargreaves, B.A., Cunningham, C.H., Nishimura, D.G., Conolly, S.M., 2004. Variable-rate selective excitation for rapid MRI sequences. Magn Reson Med 52, 590-597.

Hartung, M.P., Grist, T.M., Francois, C.J., 2011. Magnetic resonance angiography: current status and future directions. J Cardiovasc Magn Reson 13, 19.

Herscovitch, P., Raichle, M.E., 1985. What is the Correct Value for the Brain-Blood Partition Coefficient for Water? Journal of Cerebral Blood Flow & Metabolism 5, 65-69.

Hughes, T.M., Wagenknecht, L.E., Craft, S., Mintz, A., Heiss, G., Palta, P., Wong, D., Zhou, Y., Knopman, D., Mosley, T.H., Gottesman, R.F., 2018. Arterial stiffness and dementia pathology: Atherosclerosis Risk in Communities (ARIC)-PET Study. Neurology 90, e1248-e1256.

Kim, D.J., Kasprowicz, M., Carrera, E., Castellani, G., Zweifel, C., Lavinio, A., Smielewski, P., Sutcliffe, M.P., Pickard, J.D., Czosnyka, M., 2009. The monitoring of relative changes in compartmental compliances of brain. Physiol Meas 30, 647-659.

712 Kurji, A., Debert, C.T., Whitelaw, W.A., Rawling, J.M., Frayne, R., Poulin, M.J., 2006. Differences
713 between middle cerebral artery blood velocity waveforms of young and postmenopausal women.
714 Menopause 13, 303-313.

715 Lakatta, E.G., Levy, D., 2003. Arterial and cardiac aging: major shareholders in cardiovascular
716 disease enterprises: Part I: aging arteries: a "set up" for vascular disease. Circulation 107, 139-146.

717 Laurent, S., Katsahian, S., Fassot, C., Tropeano, A.I., Gautier, I., Laloux, B., Boutouyrie, P., 2003.
718 Aortic stiffness is an independent predictor of fatal stroke in essential hypertension. Stroke 34, 1203-
719 1206.

720 Lockhart, C.J., Gamble, A.J., Rea, D., Hughes, S., McGivern, R.C., Wolsley, C., Stevenson, M.,
721 Harbinson, M.T., Plumb, R.D., McVeigh, G.E., 2006. Nitric oxide modulation of ophthalmic artery
722 blood flow velocity waveform morphology in healthy volunteers. Clin Sci (Lond) 111, 47-52.

723 Lu, H., Clingman, C., Golay, X., van Zijl, P.C.M., 2004. Determining the longitudinal relaxation time
724 (T1) of blood at 3.0 Tesla. Magnetic Resonance in Medicine 52, 679-682.

725 Lu, H., Nagae-Poetscher, L.M., Golay, X., Lin, D., Pomper, M., van Zijl, P.C.M., 2005. Routine clinical
726 brain MRI sequences for use at 3.0 Tesla. Journal of Magnetic Resonance Imaging 22, 13-22.

727 Mahony, P.J., Panerai, R.B., Deverson, S.T., Hayes, P.D., Evans, D.H., 2000. Assessment of the
728 thigh cuff technique for measurement of dynamic cerebral autoregulation. Stroke 31, 476-480.

729 Mitchell, G.F., Hwang, S.J., Vasan, R.S., Larson, M.G., Pencina, M.J., Hamburg, N.M., Vita, J.A.,
730 Levy, D., Benjamin, E.J., 2010. Arterial stiffness and cardiovascular events: the Framingham Heart
731 Study. Circulation 121, 505-511.

732 Naqvi, J., Yap, K.H., Ahmad, G., Ghosh, J., 2013. Transcranial Doppler Ultrasound: A Review of the
733 Physical Principles and Major Applications in Critical Care. International Journal of Vascular Medicine
734 2013, 629378.

735 Nichols, W.W., O'Rourke, M.F., Vlachopoulos, C., 2011. McDonald's Blood Flow in Arteries:
736 Theoretical, Experimental and Clinical Principles, 6th ed. CRC Press.

737 Niwa, K., Kazama, K., Younkin, L., Younkin, S.G., Carlson, G.A., Iadecola, C., 2002. Cerebrovascular
738 autoregulation is profoundly impaired in mice overexpressing amyloid precursor protein. Am J Physiol
739 Heart Circ Physiol 283, H315-323.

740 O'Rourke, M., Stone, J., Adji, A., Kim, M.O., Li, Y., Wang, J.G., Avolio, A., Eide, P.K., Czosnyka, M.,
741 2020. The Human Systemic and Cerebral Circulations: Contrasts in Structure and Function. Artery
742 Research.

743 Pinto, J., Chappell, M.A., Okell, T.W., Mezue, M., Segerdahl, A.R., Tracey, I., Vilela, P., Figueiredo,
744 P., 2020. Calibration of arterial spin labeling data—potential pitfalls in post-processing. Magnetic
745 Resonance in Medicine 83, 1222-1234.

746 Poels, M.M., van Oijen, M., Mattace-Raso, F.U., Hofman, A., Koudstaal, P.J., Witteman, J.C.,
747 Breteler, M.M., 2007. Arterial stiffness, cognitive decline, and risk of dementia: the Rotterdam study.
748 Stroke 38, 888-892.

749 Poels, M.M., Zaccai, K., Verwoert, G.C., Vernooij, M.W., Hofman, A., van der Lugt, A., Witteman, J.C.,
750 Breteler, M.M., Mattace-Raso, F.U., Ikram, M.A., 2012. Arterial stiffness and cerebral small vessel
751 disease: the Rotterdam Scan Study. Stroke 43, 2637-2642.

752 Rabkin, S.W., 2012. Arterial stiffness: detection and consequences in cognitive impairment and
753 dementia of the elderly. J Alzheimers Dis 32, 541-549.

754 Rivera-Rivera, L.A., Schubert, T., Turski, P., Johnson, K.M., Berman, S.E., Rowley, H.A., Carlsson,
755 C.M., Johnson, S.C., Wieben, O., 2017. Changes in intracranial venous blood flow and pulsatility in
756 Alzheimer's disease: A 4D flow MRI study. J Cereb Blood Flow Metab 37, 2149-2158.

757 Robertson, J.W., Debert, C.T., Frayne, R., Poulin, M.J., 2008. Variability of middle cerebral artery
758 blood flow with hypercapnia in women. Ultrasound Med Biol 34, 730-740.

759 Shirwany, N.A., Zou, M.-h., 2010. Arterial stiffness: a brief review. Acta Pharmacologica Sinica 31,
760 1267-1276.

761 Silver, A.E., Vita, J.A., 2006. Shear Stress–Mediated Arterial Remodeling in Atherosclerosis.
762 Circulation 113, 2787-2789.

763 Suryan, G., 1951. Nuclear resonance in flowing liquids. Proceedings of the Indian Academy of
764 Sciences - Section A 33, 107.

765 Tong, Y., Frederick, B.d., 2012. Concurrent fNIRS and fMRI processing allows independent
766 visualization of the propagation of pressure waves and bulk blood flow in the cerebral vasculature.
767 Neuroimage 61, 1419-1427.

768 Verwoert, G.C., Franco, O.H., Hoeks, A.P., Reneman, R.S., Hofman, A., CM, V.D., Sijbrands, E.J.,
769 Witteman, J.C., Mattace-Raso, F.U., 2014. Arterial stiffness and hypertension in a large population of
770 untreated individuals: the Rotterdam Study. J Hypertens 32, 1606-1612; discussion 1612.

771 Viessmann, O., Moller, H.E., Jezzard, P., 2017. Cardiac cycle-induced EPI time series fluctuations in
772 the brain: Their temporal shifts, inflow effects and T2(*) fluctuations. Neuroimage 162, 93-105.

773 Wagshul, M.E., Eide, P.K., Madsen, J.R., 2011. The pulsating brain: A review of experimental and
774 clinical studies of intracranial pulsatility. Fluids and Barriers of the CNS 8, 5.

775 Warnert, E.A., Murphy, K., Hall, J.E., Wise, R.G., 2015. Noninvasive assessment of arterial
776 compliance of human cerebral arteries with short inversion time arterial spin labeling. J Cereb Blood
777 Flow Metab 35, 461-468.

778 Warnert, E.A.H., Verbree, J., Wise, R.G., van Osch, M.J.P., 2016. Using High-Field Magnetic
779 Resonance Imaging to Estimate Distensibility of the Middle Cerebral Artery. Neurodegenerative
780 Diseases 16, 407-410.

781 Whittaker, J.C., GB), Fasano, Fabrizio (Cardiff, GB), Heidemann, Robin (Litzendorf, DE), Murphy,
782 Kevin (Cardiff, GB), , Liebig, Patrick (Erlangen, DE), 2019. METHOD FOR OBTAINING MAGNETIC
783 RESONANCE IMAGING (MRI) ECHO-PLANAR IMAGE (EPI) DATA. Siemens Healthcare Limited
784 (Camberley, GB),Cardiff University (Cardiff, GB),Siemens Healthcare GmbH (Erlangen, DE), United
785 States.

786 Whittaker, J.R., Driver, I.D., Bright, M.G., Murphy, K., 2016. The absolute CBF response to activation
787 is preserved during elevated perfusion: Implications for neurovascular coupling measures.
788 Neuroimage 125, 198-207.

789 Whittaker, J.R., Steventon, J.J., Venzi, M., Murphy, K., 2020. Probing dynamic cerebral
790 autoregulation with BOLD fMRI using a thigh cuff challenge. Proc. Int. Soc. Magn. Reson. Med,
791 Virtual.

792 Wilkinson, I.B., Cockcroft, J.R., McEniery, C.M., 2015. Aortic stiffness as a cardiovascular risk
793 predictor. BMJ 351, h3764.

794 Yan, L., Liu, C.Y., Smith, R.X., Jog, M., Langham, M., Krasileva, K., Chen, Y., Ringman, J.M., Wang,
795 D.J.J., 2016. Assessing intracranial vascular compliance using dynamic arterial spin labeling.
796 Neuroimage 124, 433-441.

797 Yang, T.-H., Jo, G., Koo, J.-H., Woo, S.-Y., Kim, J.U., Kim, Y.-M., 2019. A compact pulsatile simulator
798 based on cam-follower mechanism for generating radial pulse waveforms. BioMedical Engineering
799 OnLine 18, 1.

800 Zhao, J.M., Clingman, C.S., Närväinen, M.J., Kauppinen, R.A., van Zijl, P.C.M., 2007. Oxygenation
801 and hematocrit dependence of transverse relaxation rates of blood at 3T. Magnetic Resonance in
802 Medicine 58, 592-597.

803 Zhou, G., Zhao, X., Lou, Z., Zhou, S., Shan, P., Zheng, N., Yu, X., Ma, L., 2019. Impaired Cerebral
804 Autoregulation in Alzheimer's Disease: A Transcranial Doppler Study. J Alzheimers Dis 72, 623-631.

805